Pseudo-polymorphism in layered FeS intercalates: A competition between charged and neutral guest species

Colin P. Harmer,[a,b] Saeed Kamali,[c,d] Oleg I. Lebedev,[e] Shannon J. Lee,[a,b,f] Raquel A. Ribeiro,[g] Paul C. Canfield,[b,g] and Kirill Kovnir [a,b] *

a) Department of Chemistry, Iowa State University, Ames, Iowa 50011, United States

b) Ames Laboratory, U.S. Department of Energy, Ames, Iowa 50011, United States

c) Department of Mechanical, Aerospace and Biomedical Engineering, University of Tennessee Space Institute, Tullahoma, TN 37388, United States

d) Department of Physics and Astronomy, Middle Tennessee State University, Murfreesboro, TN 37132, United States

e) Laboratoire CRISMAT, ENSICAEN, CNRS UMR 6508, 14050 Caen, France

f) Condensed Matter Physics and Materials Science Department, Brookhaven National Laboratory, U.S. Department of Energy, Upton, New York 11973, United States

g) Department of Physics and Astronomy, Iowa State University, Ames, Iowa 50011, United States

*Corresponding author: Dr. Kirill Kovnir, kovnir@iastate.edu

Abstract

Systematic synthetic studies of the formation of tetrahedral FeS-ethylenediamine intercalates resulted in synthesis of a new compound, $[Fe_{9.4(2)}S_{10}][Fe(en)_3]_{0.6(1)}\cdot en_{0.9(3)}$. The composition and complex crystal structure were determined based on a synergistic combination of elemental composition, decomposition behavior, high-resolution synchrotron X-ray diffraction and total scattering, ^{57}Fe Mössbauer spectroscopy, and electron diffraction. The structural model was derived based on a systematic comparison to the previously reported structures, $[Fe_8S_{10}]Fe(en)_3\cdot en_{0.5}$ and tetragonal FeS. The new compound has flat $Fe_{9.4}S_{10}$ layers, analogous to those in superconducting binary FeS. In the crystal structure of $[Fe_{9.4}S_{10}][Fe(en)_3]_{0.6}\cdot en_{0.9}$, the interlayer space is occupied with $[Fe(en)_3]^{2+}$ complexes and neutral ethylenediamine molecules in ~2:3 ratio. Interlayer species are not randomly oriented but ordered as evidenced by superstructural diffraction peaks in both high-resolution X-ray diffraction and electron diffraction patterns. Magnetic studies reveal no superconducting transition down to 2 K indicating that the presence of minute amounts (~6%) of iron vacancies at the Fe-S layer in $[Fe_{9.4}S_{10}][Fe(en)_3]_{0.6}\cdot en_{0.9}$ is still sufficient to shift the position of the Fermi level resulting in an adjustment of the properties. Our work shows the importance of detailed characterization of the crystal structure of intercalated compounds to understand the origin of the observed properties and develop proper structure-properties relationships.

Introduction

There is much interest in defining the interplay of structure and properties in iron-chalcogenide superconducting materials. The parent superconductors, tetragonal iron sulfide (mackinawite) and selenide (β-FeSe) exhibit superconductivity at 5 K and 8 K, respectively.[1-2] Numerous studies have shown that intercalation can change the bulk properties, and in some cases, intercalation results in the many-fold increase of onset superconductivity temperatures (T_c) up to 45 K.[3-6] These intercalated iron chalcogenides follow a common structural motif with Fe-*Ch* (*Ch* = S, Se, Te) layers, made of a square net of Fe$Ch_{4/4}$ edge sharing tetrahedra, separated by interstitial species. The interstitial space is filled with neutral or low net charge species,[7] including electropositive cations, metal ammonia/amide/amine complexes, LiOH layers, and organic molecules such as diamines as schematically shown in **Figure 1**.

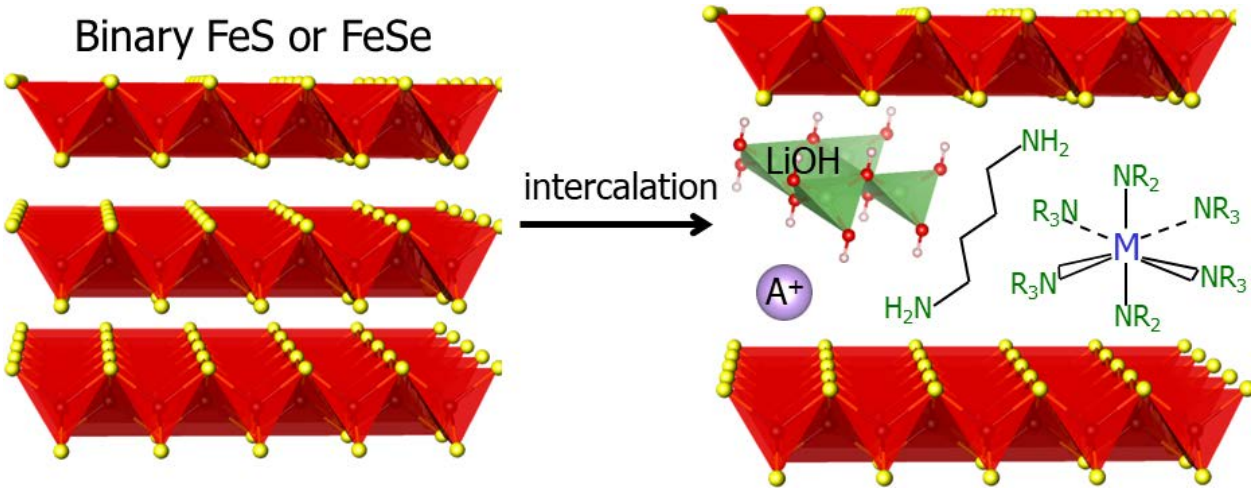

Figure 1. A schematic representation of the intercalation into binary FeS and FeSe with several possible interlayer species which are not necessarily mutually exclusive. Fe: black; S or Se: yellow; *A* = Li-Cs, and NH_4; *M* = transition or electropositive metal of Groups 1 and 2; *R* = H, C_xH_y.

In general, researchers have focused on a few key aspects that seem to play a significant role in the suppression or enhancement of the superconducting properties of intercalated

compounds. These include, the interlayer distance, the regularity of the Fe*Ch*$_4$ tetrahedra, and the parameters which affects the density of states at the Fermi level, such as the average Fe oxidation state, and the concentration of Fe vacancies in the Fe-*Ch* layer.[7] A complete description of the Fe-*Ch* layer as well as the intercalate is required to accurately link these structural aspects to a material's bulk properties. Whereas interplanar van der Waals stacking is ideal for diverse intercalation, it can limit crystal quality and in turn complicate the structure-properties analysis. In most cases, the structure of the intercalated polycrystalline samples is determined by fitting a model against powder diffraction data. In some cases, like alkali-amide and alkali-hydroxide intercalations, powder diffraction can accurately model the crystal structure.[4, 8] In both cases X-ray powder diffraction was best to model the structure of the Fe-*Ch* fragment, but neutron powder diffraction was required to elucidate the structure of the intercalate containing light elements, such as N, O, and H.[9-10]

However, in many other cases, powder diffraction alone cannot accurately describe the full crystal structure. For example, a variety of Fe*Ch* have been investigated with ethylenediamine as the primary intercalate. Across these seemingly related phases, some exhibit bulk superconductivity whereas others do not show any superconducting transition down to 2 K.[11-16] These ethylenediamine intercalated samples tend to have a high degree of disorder, generally resulting in low quality powder X-ray diffraction data. Additionally, the intercalate, made of weak X-ray scatterers, contributes a minute fraction to X-ray powder diffraction peak intensities. Neutron diffraction studies are hampered with high cost of commercial deuterated d^8-ethylenediamine given the amounts required for solvothermal experiments.[17] As a result, the Fe*Ch* layer can be reasonably modeled by powder X-ray diffraction but any intercalate structure can be thought of as more a qualitative, schematic picture, where many solutions can fit the data.

Overall, the total Fe:*Ch* ratio is noted as a significant parameter defining magnetic and/or superconducting properties as it was directly related to the stoichiometry of the Fe-*Ch* tetrahedral layer and used to evaluate whether any Fe vacancies are present. However, relying on the total Fe:*Ch* ratio alone can be deceiving, because the interlayer space may contain chelating Fe complexes, such as $[Fe(en)_3]^{2+}$ (en = ethylenediamine), which impacts the overall Fe:*Ch* ratio, meaning a compound with an overall 1:1 Fe:*Ch* composition that could still be iron deficient at the Fe-*Ch* layer.[11,18] Moreover, we have shown that ethylenediamine is capable of leaching Fe from the stoichiometric FeS layers to form $[Fe(en)_3]^{2+}$ *in situ*.[17] Absence of high-quality crystal structure data due to the low crystallinity of the intercalated phases together with potential disorder in the interlayer space and Fe vacancies in the Fe-*Ch* layers prevent development of structure-property relationships for this class of compounds. To better pinpoint the causes for the observed range of property changes it is crucial to not only know the structure but also systematically alter the structure and composition to better relate the structure and properties.

Intercalation of en into the interlayer space of FeS leads to the formation of ordered $[Fe_8S_{10}]Fe(en)_3 \cdot en_{0.5}$ compound. In this case, both charged $[Fe(en)_3]^{2+}$ coordination complexes and neutral en molecules jointly occupy the interlayer space in 2:1 ratio.[17] Presence of the charged complexes leads to the formation of intralayer Fe vacancies, increasing the Fe average oxidation state to +2.25, and puckering of the Fe-S layers. Our extensive synthetic exploration of Fe-S-en system reveals an existence of another compound which first was assumed to be a polymorphic analogue of $[Fe_8S_{10}]Fe(en)_3 \cdot en_{0.5}$ due to overall similarity of powder X-ray diffraction patterns. Whereas both phases resemble a related general structure, with $Fe_{1-x}S$ layers intercalated by $[Fe(en)_3]^{2+}$ complexes as well as free ethylenediamine, close examination reveals clear contrast in their structure and properties. Comprehensive synthetic and structural explorations by a synergistic

combination of synchrotron powder X-ray diffraction and total scattering, electron diffraction, ^{57}Fe Mössbauer spectroscopy, energy dispersive X-ray spectroscopy (EDS), and TGA/FTIR show that in the new compound $[Fe_{9.4}S_{10}][Fe(en)_3]_{0.6}\cdot en_{0.9}$ the significant fraction of charged complexes is replaced with neutral en resulting in a 2:3 ratio. This results in the decrease of the overall charge of the intercalated species, suppression of the Fe vacancies and the reduction of Fe atoms in the FeS layer leading to flat structure of the layer, making it similar to that of binary FeS. Magnetic properties of $[Fe_{9.4}S_{10}][Fe(en)_3]_{0.6}\cdot en_{0.9}$ are drastically different from those for $[Fe_8S_{10}]Fe(en)_3\cdot en_{0.5}$. Synthesis, structure, and magnetic properties of both pseudo-polymorphic layered phases in the Fe-S-en systems are reported in this work.

Experimental Section

Synthesis

Starting materials were used as received unless otherwise noted: elemental iron (Alfa Aesar, >99.5%), sulfur powder (Alfa Aesar, 99.5%), ammonium chloride (Alfa Aesar, 99.5 %), ethylenediamine (Alfa Aesar, 99%), ethanol (Fischer, 200 proof). Iron powder was reduced before use under H_2 flow at 700 °C for 5 hours then sieved through 100 mesh. Ethylenediamine and ethanol were argon degassed and dried over molecular sieves in a solvent purification system (Pure Process Technology) connected directly to an argon filled glovebox. All sample manipulations were performed under argon unless otherwise noted.

Solvothermal Synthesis

Caution: solvothermal vessels may develop high autogenic pressure which may result in the release of hot pressurized hazardous ethylenediamine vapor during reaction which may cause severe burns. Splashing of the solvent may occur upon opening the autoclaves. Wearing of proper

protective equipment including face-shields, long-sleeve gloves, and tight-cuff lab coats and placing furnaces in well-ventilated spaces such as fume hoods is highly recommended.

$[Fe_8S_{10}]Fe(en)_3 \cdot en_{0.5}$, **1**, was synthesized from Fe (0.5 mmol), S (0.5 mmol), and NH_4Cl (4 mmol) in 10 mL ethylenediamine (0.43 filling fraction) loaded in 23 mL PTFE lined stainless steel autoclaves in an argon glovebox. The autoclaves were then sealed, removed from the glovebox, and placed in a preheated furnace at 200 °C for 3-7 days. Autoclaves were removed from the furnace, allowed to cool under ambient conditions for 1-2 hours, then transferred into the glovebox. Samples were vacuum filtered, washed with EtOH (2×150mL), then dried in the glovebox antechamber for 1-24 h. The relatively large volume of EtOH was required to ensure complete removal of $Fe(en)_3Cl_2$ admixture.[17]

$[Fe_{9.4}S_{10}][Fe(en)_3]_{0.6} \cdot en_{0.9}$, **2**, was synthesized from Fe (0.5 mmol), S (0.5 mmol), and no NH_4Cl was added to the reaction mixture. Fe and S were combined with 17 mL of ethylenediamine (0.73 filling fraction) in a 23 mL PTFE lined stainless steel autoclave, which was sealed and placed in furnace pre-heated to 200 °C and kept at this temperature for 7 days. Sample prep and workup was conducted under the same air/water free conditions used for **1**. For some experiments, residual Fe powder was mechanically removed with a magnet as previously described.[17] This procedure of admixture Fe removal accompanied with removal of a significant part of sample stuck to Fe particles. The removal was applied for samples where elemental iron would have an impact on characterization such as EDS and SQUID measurements. Since elemental Fe signal is well-resolved in ^{57}Fe Mössbauer spectra the magnet purification procedure was not applied for sample analyzed with Mössbauer spectroscopy. Estimation of the residual Fe content from magnetization data and Rietveld refinement of synchrotron PXRD indicated that 1.2-1.5 wt.-% of Fe remains in the sample **2** after magnet Fe removal procedure. In the manuscript, it is indicated when the Fe

removal procedure was applied. Mechanical separation was not required for compound **1** samples as all elemental Fe was consumed by excess NH_4Cl present, forming $Fe(en)_3Cl_2$.

Elemental analysis

Elemental analysis was conducted on an FEI Quanta 250 field emission-scanning electron microscope (SEM) with EDS detection (Oxford X-Max 80) and Aztec software. Residual Fe was mechanically removed from compound **2** sample prior to the measurements. Samples were cold pressed into 8 mm diameter pellets with 1 ton applied pressure, then polished with 1200 grit paper. The sample was mounted onto carbon tape and dusted prior to measurement. The energy of the electron beam used was 15 keV.

Thermal Decomposition

Simultaneous thermogravimetric analysis (TGA) and differential scanning calorimetry (DSC) coupled with Fourier transformed infrared (FTIR) spectrometry was performed on a Netzsch STA449F1 TGA/DSC system using Al_2O_3. Temperature profile followed an isothermal step at 40 °C for 5 min, then 10 °C/min ramp to 600 °C under a 10 mL/min flow of high purity Ar. The system was coupled to a Bruker Tensor 10 FTIR spectrometer for evolved gas analysis. Samples were exposed to air between initial mass calibration and measurement (~2 h).

X-ray structure determination

Laboratory powder X-ray diffraction patterns collected on a Rigaku 600 Miniflex with Cu-K_α radiation (λ = 1.54059 Å) and Ni-K_β filter were used for the initial crystalline phase identification. High-resolution X-ray powder diffraction patterns were collected (λ = 0.412819 Å) at beamline 11-BM-B at the Advanced Photon Source at Argonne National Laboratory (APS ANL). FOX and GSAS-II softwares were used for average structure determination with final Rietveld refinement in GSAS-II.[19-20] Synchrotron X-ray total scattering data were collected at 11-

ID-B (APS ANL) and 28-ID-1 (National Synchrotron Light Source II at Brookhaven National Laboratory) for compounds **1** and **2,** respectively. Total scattering data were reduced in GSAS-II and then corrected for background and Fourier transformed in PDFgetX3 software.[20-21] Local structures were refined against the pair distribution functions (PDFs) in PDFgui software.[22]

Transmission Electron Microscopy

High-resolution TEM (HRTEM) and electron diffraction (ED) studies were performed using a Tecnai G2 30 UT (LaB6) microscope operated at 300 kV with 0.17 nm point resolution and equipped with an EDAX EDX detector.

^{57}Fe Mössbauer spectroscopy

^{57}Fe Mössbauer spectroscopy measurements were performed at 6 K, 100 K, and 293 K using an MS4 spectrometer operating in the constant acceleration mode, in connection to a Janis closed cycle refrigerator, in transmission geometry. A 50 mCi ^{57}Co in Rh held at room temperature (RT) was used as a source. All centroid shifts, δ, are given with respect to metallic α-iron measured at RT. Using Recoil software,[23] the spectra were least square fitted by a Lorentzian analysis to extract hyperfine parameters, which are δ, quadrupole splitting/quadrupole shift ($\Delta E_Q/\varepsilon$), magnetic hyperfine field (B_{hf}), fullwidth at half maxima (Γ), and intensities (I).

Magnetic properties

Magnetic measurements were performed on polycrystalline samples with a Quantum Design SQUID MPMS magnetometer. Residual Fe was mechanically removed from compound **2** prior to the measurements. The temperature-dependence of the magnetization was studied in different applied magnetic fields of 0.1-7 T. Isothermal field-dependence of the magnetization was studied in 0-5 T fields.

Results and Discussion

Solvothermal synthesis can yield two phases in the Fe-S-en system. While the powder X-ray diffraction patterns have some similarities, those phases are not polymorphs but rather two unique compounds with different structures of the Fe-S tetrahedral layer, different compositions, and different properties. We previously described the structure of $[Fe_8S_{10}]Fe(en)_3 \cdot en_{0.5}$ as determined by single crystal XRD, which will be referred to as compound **1**.[17] This report focuses on the structure determination of a pseudo polymorphic analogue, compound **2**. Although the synthesis for **2** does not yield single crystals suitable for diffraction experiment, we synergistically applied PXRD, ED, EDS, TGA/DSC, ^{57}Fe Mössbauer spectroscopy, and X-ray total scattering pair distribution function analysis to determine the composition and crystal structure of **2**. Compound **1**, $[Fe_8S_{10}][Fe(en)_3] \cdot en_{0.5}$ is composed of $[Fe_8S_{10}]^{2+}$ puckered layers intercalated by $[Fe(en)_3]^{2+}$ octahedral complexes and free ethylenediamine (**Figure 2b**). Compound **2** has a smaller concentration of Fe vacancies in a flat Fe-S layer with composition $[Fe_{9.4}S_{10}]$ (**Figure 2c**) and in turn less intercalated $[Fe(en)_3]^{2+}$ complexes and more neutral en molecules resulting in an average composition as $[Fe_{9.4(2)}S_{10}][Fe(en)_3]_{0.6(1)} \cdot en_{0.9(3)}$.

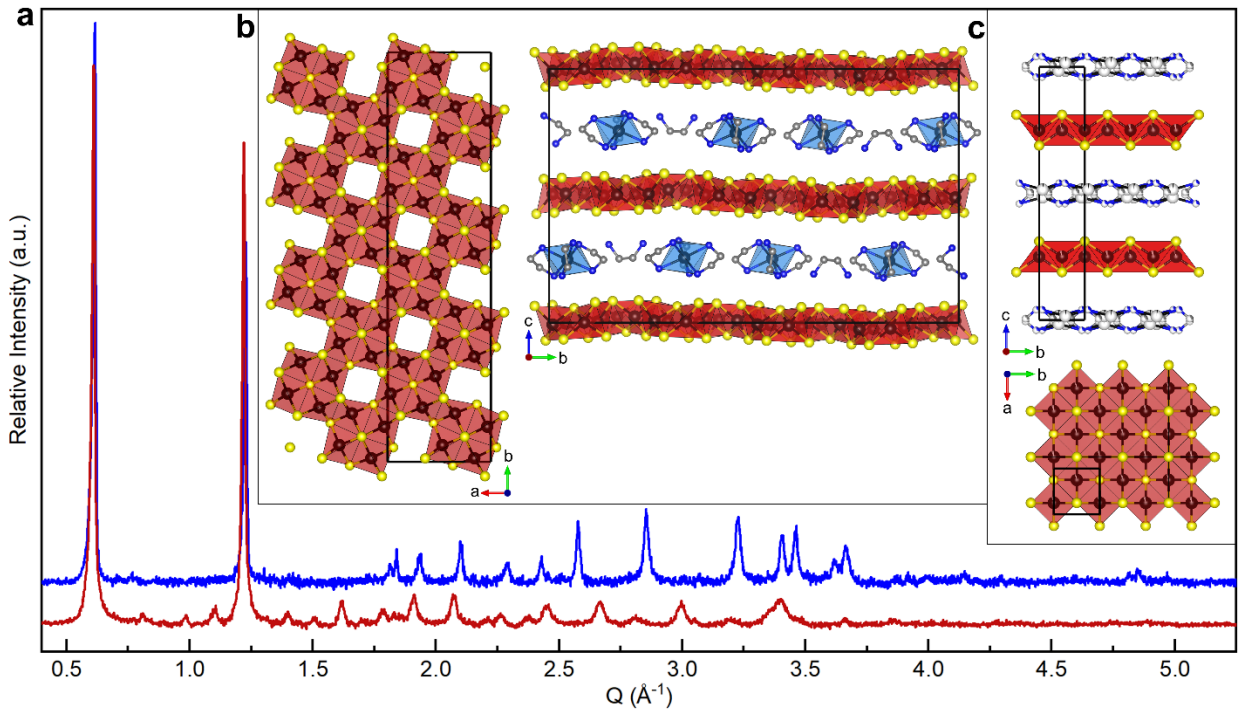

Figure 2. (a) *Benchtop PXRD patterns of compounds* ***1*** *(red) and* ***2*** *(blue). Data are normalized and background subtracted for clarity (Cu* K_α*,* λ *= 1.54059 Å). Crystal structures of* ***(b)*** *compound* ***1****,* $[Fe_8S_{10}]Fe(en)_3 \cdot en_{0.5}$ *and* ***(c)*** *compound* ***2****,* $[Fe_{9.4(2)}S_{10}][Fe(en)_3]_{0.6(1)} \cdot en_{0.9(3)}$ *(*$A2_122$ subcell*) as viewed along [100] and top view along [001] of Fe-S layer along ab-plane. Fe: black; S: yellow; N: blue; C: grey; hydrogens are omitted for clarity.*

Primary analysis from benchtop PXRD reveals a clear contrast between the two compounds (**Figure 2a**). While both diffraction patterns suggest layered structures with similar interlayer distance, there are large differences in the higher *Q* peaks which rely heavily on the structure within the Fe-S layer. In **1** the puckered Fe-S sheets lead to broad diffraction peaks whereas in **2** the higher angle peaks are much sharper, suggesting a more regular structure within the Fe-S layer.

Before exploring the composition and structure, a complete phase separation of the two polymorphs was ensured. As noted in the experimental section, compound **1** forms in the presence of mineralizer (e.g., NH_4Cl), whereas compound **2** can only form in mineralizer-free conditions. Moreover, it seems that using elemental Fe as starting material is a prerequisite to form compound **2** because all attempts to form compound **2** using soluble Fe^{2+} precursors, such as $FeCl_2$, failed. We hypothesized that an equilibrium with unreacted metallic Fe during the synthesis is required to provide a reducing environment and stabilize compound **2**. This assumption is supported with lower average oxidation state of tetrahedral Fe in compound **2** (Fe^{2+}) as compared to that in compound **1** ($Fe^{2.25+}$) – see discussion of Mossbauer results below.

EDS elemental analysis confirmed the absence of Cl in both compounds. Throughout synthetic optimizations it was found the total filling fraction of ethylenediamine in the autoclave affected the purity and crystallinity of **2**. The original method using 10 mL of ethylenediamine (43% filling fraction) led to a mixture of **1** and **2**. An increase of the filling fraction to 17 mL ethylenediamine (73% filling fraction) was required to synthesize single phase sample of **2**, along with a small but unavoidable elemental Fe admixture, as determined by high resolution synchrotron PXRD.

Figure 3a compares high resolution PXRD patterns from **1** (red), as-synthesized **2** (blue), and a biphasic mixture (black). These high-resolution patterns first reveal a small, 0.8%, interlayer compression from 10.24 Å in **1** to 10.16 Å in **2**, as highlighted in **Figure 3b**. The powder pattern plotted in black shows a clear splitting of the (004) diffraction peak at 1.23 $Å^{-1}$ suggesting the presence of both compounds in that sample. It should be noted that the 0.1 Å interlayer compression, (< 0.02 $Å^{-1}$ at (004) peak) is not well resolved using a conventional benchtop diffractometer and requires high resolution synchrotron PXRD. **Figure 3c** shows some key

differences in the higher angle peaks. Although **1** and **2** have numerous overlapping peaks, compound **1** can be identified by peaks at 1.6 and 3.0 $Å^{-1}$ and compound **2** is readily identified by a peak at 3.2 $Å^{-1}$, in addition to peaks of elemental Fe as indicated in the **Figure 2c**. Those characteristic peaks were used to identify corresponding phases with routine benchtop PXRD experiments.

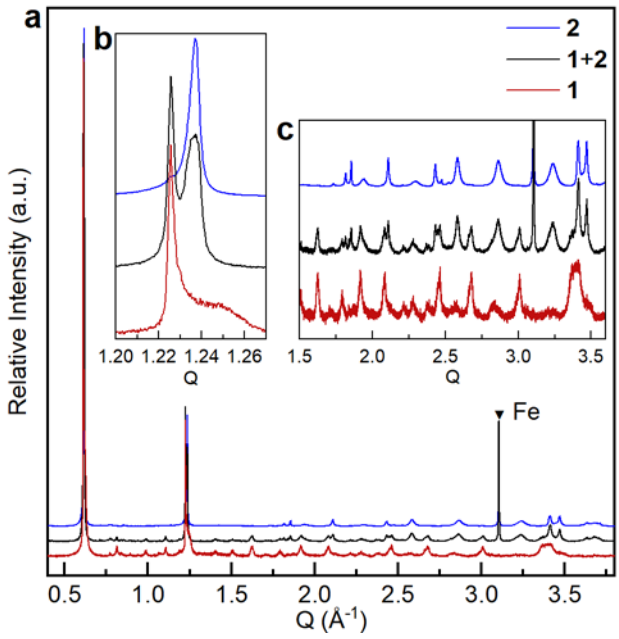

Figure 3. (a) *High resolution synchrotron PXRD of compounds **1** (red), **2** (blue), and a biphasic mixture of both (black) collected at 100 K.* ***(b)*** *Left inset reveals compression of interlayer spacing (004).* ***(c)*** *Right inset highlights differences in less intense peaks. Residual elemental Fe peak indicated by black triangle.*

The total Fe-S content for compound **2** after magnetic cleaning was analyzed with EDS using **1** as a standard (**Figure S1**). Pellets of both compounds were loaded in a custom air-free holder and analyzed in tandem to aid comparison. EDS provided an average Fe-S composition normalized to 10 S atoms of $Fe_{9.6(2)}S_{10}$ for **1** and $Fe_{10.7(2)}S_{10}$ for **2**. In comparing $Fe_{9.6(2)}S_{10}$ to our

single crystal data for **1**, $[Fe_8S_{10}]Fe(en)_3 \cdot en_{0.5}$, the Fe content may be overestimated by *ca.* 7 %. Thus, using **1** as a standard an average Fe-S composition in **2** was estimated as $Fe_{10.0(2)}S_{10}$. Additionally, EDS indicated a lower N content for compound **2** as compared to compound **1**, 5.6 vs. 7 per 10 S atoms, respectively. The observed difference in Fe content between compounds **1** and **2**, 1 out of 10 atoms, is significantly larger than the e.s.d. of the measurements, 0.2. No elemental Fe admixture was detected in the EDS measurements. The presence of an Fe metal admixture underneath the surface of the studied phase may potentially obscure the measurements. Even under the assumption that Fe metal contributed to the signal, the observed Fe weight difference for the proposed compositions of **1** and **2** is 2.5 wt.-% which is larger than the estimate of the Fe metal content, 1.2-1.5 wt.-%.

While EDS provides the overall Fe-S composition in each compound, it does not differentiate between intralayer and intercalated Fe atoms. Overall composition of Fe_9S_{10} for **1** comes from Fe_8S_{10} composition of the layer plus one $[Fe(en)_3]^{2+}$ intercalated complex. Similarly, compound **2** may be best described at $[Fe_{10-z}S_{10}] \cdot [Fe(en)_3]_z$. As such, we utilized ^{57}Fe Mössbauer spectroscopy to probe the chemical environment of Fe, further details are discussed below. The room temperature (RT) Mössbauer spectrum for **1** has a clear signal for Fe^{2+} in an octahedral environment with an overall relative intensity of 11%, which is in good agreement with the $[Fe_8S_{10}]Fe(en)_3 \cdot en_{0.5}$ structure. Similarly, octahedral Fe^{2+} signal was detected for compound **2** thus confirming that $[Fe(en)_3]^{2+}$ complex is present in the interlayer space. The relative intensity of such signal was 6% suggesting a composition $[Fe_{9.4(2)}S_{10}] \cdot [Fe(en)_3]_{0.6}$ with the potential for extra free ethylenediamine molecules. Sample of compound **2** for Mössbauer spectroscopy was not magnetically cleaned and the total amount of Fe admixture can be estimated based on the signal of elemental Fe, which comprises 11% of the total intensity. This corresponds to 6.1 wt.-% of

elemental Fe in the as synthesized sample, which can be further reduced to 1.2-1.5 wt.-% via magnetic separation.

After establishing the composition of **2** as $[Fe_{9.4(2)}S_{10}]\cdot[Fe(en)_3]_{0.6}\cdot en_x$, TGA-DSC coupled with FT-IR was used to evaluate the ethylenediamine content. Powdered samples were heated under vacuum from RT to 600 °C at 10 °C/min rate (**Figures 4 and S2**). Upon heating, samples release ethylenediamine and decompose into binary iron sulfides. FT-IR spectroscopy confirms ethylenediamine as the major component of the evolved gas. The absorbance at 770 cm^{-1} (ethylenediamine's most intense peak) versus temperature was used to correlate mass loss to ethylenediamine evolution (**Figure 4**). Both compounds show evaporation of physisorbed water and CO_2 at temperature below 125 °C and main weight loss due to en elimination in 125-350 °C range according to FT-IR (**Figure S2**).

The DSC plot of **1** (**Figure 4a**) shows two distinct endothermic features at 230 °C and 280 °C in alignment with ethylenediamine evaporation. We attribute the 230 °C feature to loss of 0.5 equivalents of free ethylenediamine, while the 280 °C feature indicates loss of the more tightly bound ethylenediamine from the $[Fe(en)_3]^{2+}$ complex. This assignment is justified through the relative heat flow and ethylenediamine evolution at each temperature, because 6:1 ratio is expected for ethylenediamine from the intercalated complex *vs.* free ethylenediamine.

In contrast to **1**, the heat flow of **2** (**Figure 4b**) shows three relatively broad endothermic features at 180 °C, 220 °C, and 280 °C. Additionally, evolved gas FT-IR reveals a continuous release of ethylenediamine maximizing at *ca.* 220 °C. This suggests that **2** has larger ratio of free ethylenediamine to coordinated ethylenediamine.

Based on FTIR and DSC signals, the total ethylenediamine content can be estimated by mass loss from 125 °C to 350 °C. Compound **1** loses 23% of its mass across this range resulting

in $Fe_9S_{10}en_{4.1}$ composition for **1**. Compound **2** loses 19% of its mass across the same temperature range. From EDS+Mössbauer we assume the sample to be $[Fe_{9.4}S_{10}][Fe(en)_3]_{0.6}\cdot en_x$ + 6.1 wt.-% of elemental Fe. This reveals an approximate value of x as = 3.7. TGA is expected to overestimate ethylenediamine content from ethylenediamine and CO_2 on the surface and potential S evaporation. Although the absolute ethylenediamine content may be overestimated, each sample was prepped and run under identical conditions. Using the known composition from crystal structure, ethylenediamine content in **1** ($Fe_9S_{10}en_{3.5}$) as a standard, corrected composition of **2** can be estimated as $Fe_{10}S_{10}en_{2.7(3)}$, corresponding to $[Fe_{9.4}S_{10}][Fe(en)_3]_{0.6(1)}\cdot en_{0.9(3)}$. The total corrected ethylenediamine content aligns with derived from EDS Fe-S-N content, $Fe_9S_{10}N_7$ vs. $Fe_{10.0(2)}S_{10}N_{5.6}$ for **1** and **2** (**Figure S1**).

In **Figure 4c** the powder X-ray diffraction data on the decomposition products of each sample after DSC-TGA are shown and provides additional evidence for Fe-S composition determined by EDS. Both phases decompose to hexagonal $Fe_{1-z}S$ binaries with visible differences: **1** decomposes to iron deficient pyrrhotite ($P6_3/mmc$, a = 3.4495(3) Å, c = 5.7569(4) Å), while **2** decomposes to the superstructural variant, troilite ($P\bar{6}2c$, a = 5.9639(8) Å, c = 11.6825(9) Å). Elemental Fe admixture stays intact in the sample of compound **2**. *Keller-Besrest et al*. show that the substructure c-parameter of $Fe_{1-z}S$ decreases with increasing iron vacancies and further note superstructural ordering can only exist for $z \leq 0.05$.[24] Thus, the superstructural ordering and larger reduced subcell c-parameter (5.8412 Å) show that the decomposition product of **2** has less Fe vacancies than that of **1** in line with determined $Fe_{10}S_{10}$ composition for compound **2**. Combining our results of PXRD, EDS, Mössbauer spectroscopy, and TGA-DSC, we determine the general composition for **2** as $[Fe_{9.4(2)}S_{10}][Fe(en)_3]_{0.6(1)}\cdot en_{0.9(3)}$, composed of $[Fe_{9.4}S_{10}]^{1.2-}$ layers intercalated by $[Fe(en)_3]^{2+}$ and free ethylenediamine.

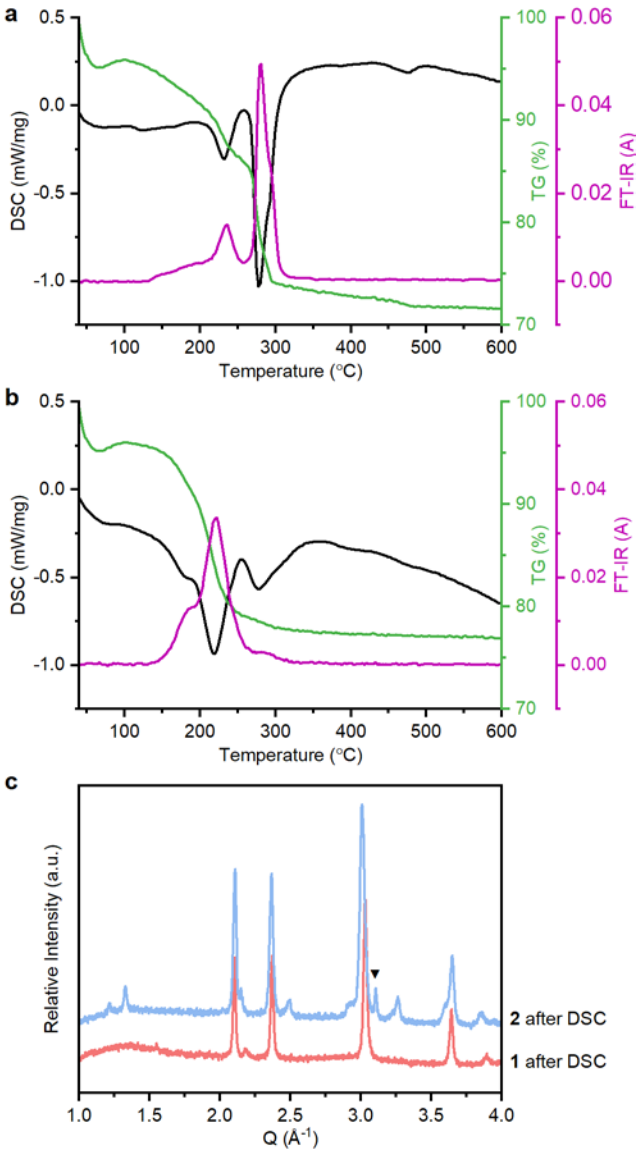

Figure 4. (a),(b) *DSC/TGA and concurrent evolved gas FT-IR analysis for powdered* ***1*** *and* ***2,*** *respectively. DSC plot (black) given as heat flow vs. temperature. TGA plot (green) indicates mass loss vs. temperature. Low temperature (<125 ℃) weight variations are due to desorption of physiosorbed moisture and* CO_2*. FT-IR plot (purple) reveals absorbance from evolved gas at 770* cm^{-1} *vs. temperate.* ***(c)*** *Benchtop PXRD patterns collected after DSC. Black triangle indicates residual Fe, which was present before and after DSC for* ***2****.*

X-ray total scattering pair distribution function (PDF) analysis provides insight into the local structure of each compound and is a good starting point to generate the structural model of compound **2**. PDFs of the two samples are directly compared in **Figure 5**. In general, despite an overlap of peak positions, especially at lower interatomic distances (r < 10 Å), a significant contrast in peak shape is observed. The peak centered at 2.3 Å, representing the Fe-S bond, shows large overlap and can be used as a reference point for direct comparison. Beyond the Fe-S bond distance, broad peaks are present in the PDF of **1** while the peaks in PDF of compound **2** remain relatively sharp out to 30 Å.

The broad peaks of compound **1** stem from the puckered nature of the $[Fe_8S_{10}]^{2+}$ layers resulting in a large distribution of interatomic distances. In compound **1**, 20% iron vacancies and the puckered nature of the Fe-S layer cause significant distortion in the FeS_4 tetrahedra with ∠S−Fe−S spanning 99° to 123°.[17] Furthermore, the Fe···Fe next nearest neighbors distances range from 3.43 Å to 3.98 Å. In contrast, compound **2** has only 6% iron vacancies within the $Fe_{9.4}S_{10}$ layer which we expect to lead to more regular, mackinawite-like, layers.[25] This is exemplified in the comparatively sharp PDF peaks in compound **2**, indicating a smaller distribution of interatomic distances. Additionally, we see compression of the Fe···Fe nearest neighbor distances from 2.77 Å in **1** to 2.61 Å in **2**, aligning close to the 2.60 Å Fe···Fe nearest neighbor distances in mackinawite.[2] Interestingly, adjustment of the interlayer distance in mackinawite crystal structure to 10.2 Å provides a crystal model which fits reasonable well to the PDF for compound **2** out to r = 10 Å.

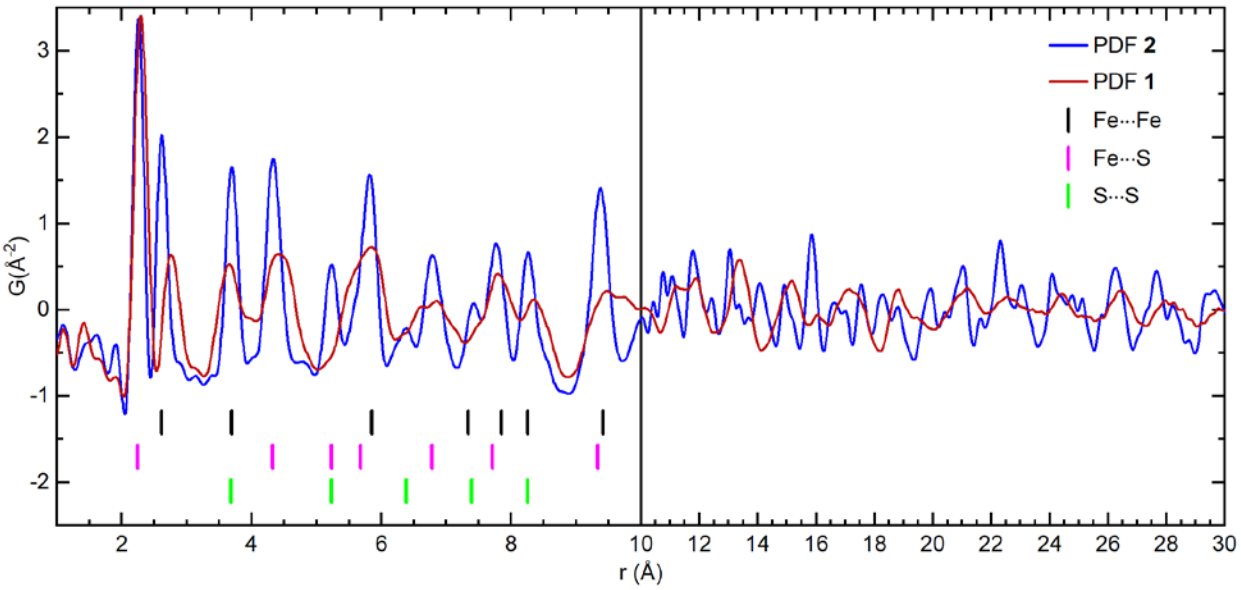

Figure 5. *Experimental X-ray PDFs from* ***1*** *(red) and* ***2*** *(blue). Rescaled x-axis at 10 Å for clarity. Ticks indicate interatomic Fe···Fe (black), Fe···S (magenta), S···S (green) distances (<10 Å) for final determined structure of compound* ***1****.*

The average structure of compound **2** was solved and refined against high-resolution synchrotron PXRD data using compositional constrains guided by the results of EDS, Mössbauer spectroscopy, and TGA-DSC. Sample was purified with a magnet prior to the measurements. Unit cell and atomic sites were initially determined via a reverse Monte Carlo approach in FOX,[19] then refined by the Rietveld method in GSAS II.[19-20] The majority of the diffraction peaks can be indexed in the $A2_122$ space group (non-standard settings of $C222_1$, No. 20), with unit cell parameters a = 3.70 Å, b = 3.69 Å, and c = 20.51 Å. Atomic coordinates (**Table S3**) were determined by first adding one Fe and one S site to describe the $Fe_{9.4}S_{10}$ layer, with the Fe site occupancy fraction set to 0.94 as per the determined composition. These coordinates, at 4*b* Wycoff sites, are consistently found across multiple iterations and the resulting calculated pattern fits the PXRD data well. The atomic coordinates of intercalated Fe and ethylenediamine are challenging

to determine. First, the unit cell in the *ab* plane is too small to accurately describe any intercalated $[Fe(en)_3]^{2+}$ complex. Second, the intercalate is composed of relatively weak X-ray scatterers, H, C, and N as well as a small fraction of Fe and is possibly disordered. As such, the intralayer site coordinates were locked before adding one Fe, one N, and one C site, occupancies adjusted to match the $Fe_{9.4}S_{10}Fe_{0.6}N_6C_6$ composition. The interlayer coordinates were then refined across multiple iterations before performing the global refinement of the whole structure. The final solution was refined through the Rietveld method (**Figure 6**). This sample had some residual Fe impurity which refined to 1.21(1) wt. %, in agreement with magnetization data suggesting 1.5 wt. %. The structure was further verified by fitting the PDF of compound **2** in PDFgui (**Figure S4, Table S3**).[22] The final fit, from r = 1-30 Å, converged to R_w = 21.6%. For comparison, compound **1**, fit against its known structure, converged to R_w = 21.0 %, and reported PDF fits of crystalline mackinawite have R-values of 20-30%.[25] Details of the Rietveld refinement and PDF fit are provided in **SI**.

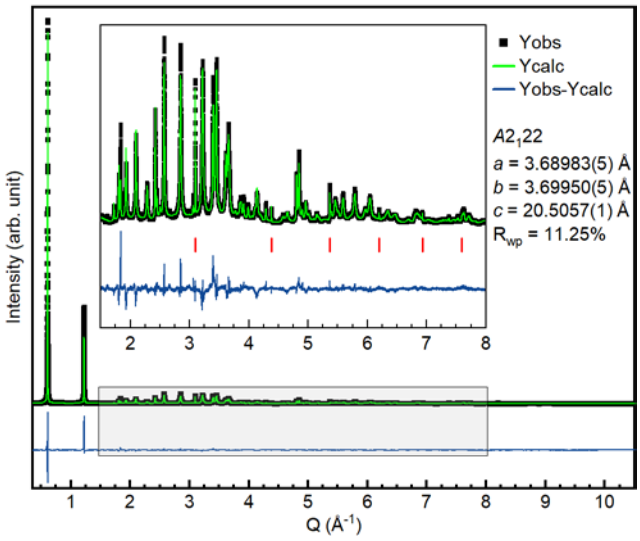

Figure 6. *Rietveld refinement on high resolution synchrotron PXRD data of compound* ***2*** *(APS 11-BM-B, λ = 0.45791 Å). Inset shows the enlarged part at high-Q range of 1.5-8 Å^{-1}. Red ticks indicate elemental Fe impurity.*

The refined crystal structure of compound **2** contains flat FeS layers composed of only of one type of FeS_4 tetrahedra with two different Fe-S distances of 2.230 Å and 2.249 Å and S-Fe-S angles of 108.6-111.6°. These tetrahedra are more regular than such units present in the puckered layers of compound **1** but still are slightly distorted in comparison to FeS_4 tetrahedra in mackinawite.[26] In the latter, the S-Fe-S angles vary in a similar range but only one type of Fe-S distances is present, 2.231 Å. In compound **2** within the flat Fe-S layer almost a square net of Fe atoms with Fe-Fe distance of 2.613 Å and angles of 89.83° and 91.15° is present. In comparison, in mackinawite a regular square Fe net with the Fe-Fe distance of 2.601 Å and 90.00° angles is present. Thus, the Fe-S part of the crystal structure of compound **2** is a slightly distorted orthorhombic version of mackinawite. For β-FeSe an orthorhombic distortion to *Cmma* can be induced either by lowering temperature or by applying high pressure. However, in the reported *Cmma* structures all Fe-Se bonds remain essentially the same length but Fe-Fe distances in the flat layer become inequivalent along two orthogonal directions.[27,28] Compound **2** exhibits different type of the orthorhombic distortion of Fe-S layer.

The base cell of 3.69×3.70×20.51 $Å^3$ is insufficient to properly describe interstitial species in the structure of compound **2**, both $[Fe(en)_3]^{2+}$ complexes and free en molecules are highly disordered. $[Fe(en)_3]^{2+}$ complex with D_3 (32) local symmetry may be present in solution as Δ- or Λ-isomers. Crystallization of such complexes without specific directing agents is expected to result in the formation of crystal structures with both isomers present in 1:1 ratio in analogy with centrosymmetric structures of compound **1** and chain-like Fe-Se compounds, or even in the polar but not chiral structure of $[Co(en)_3](CoS)_{12}\cdot en$.[14,17,29,30] The structure of compound **2** was solved in the chiral space group $A2_122$ implying only one type of stereoisomer of $[Fe(en)_3]^{2+}$ to be present.

Without the full solution of the crystal structure in the supercell discussed below the presence of only one $[Fe(en)_3]^{2+}$ isomer is an assumption.

The refined structure of compound **2** fits all intense peaks in the diffraction pattern but some minute peaks, corresponding to larger *d*-spacings (*ca*. 4-10 Å), cannot be indexed by a 3.69×3.70×20.51 $Å^3$ cell. Further, the residual peaks from synchrotron PXRD data of compound **2** are not indexed by the calculated pattern of compound **1**, thus indicating of a possibility for superstructural ordering. The residual peaks are best indexed by a $4a\times3b\times c$ supercell, suggesting ordering along the *ab*-plane (**Figure 7a**). Electron diffraction was used to further probe the superstructural ordering. As shown in **Figure 7b**, the $[30\bar{1}]$ zone axis, indexed in the $A222_1$ base cell (red), fits the brightest spots at small *d*-spacings, but cannot be fully indexed in the base cell. The interlayer distances of those superstructural spots in the ED patterns corresponds to a $4a\times3b\times c$ supercell (indexed in green). However, there remain unindexed peaks, suggesting further ordering along the *a*-axis. Additionally, across multiple ED images at least two types of superstructural ordering were observed, $4a\times3b\times c$ and $2a\times2b\times c$, but no single supercell can index all images (**Figure S5**). While PXRD reveals the average structure of all crystallites, ED probes individual domains which can vary within a sample. We hypothesized, that local ordering of the two types of intercalated species, $[Fe(en)_3]^{2+}$ complexes and neutral en molecules, yields different ordered superstructures on the local scale as evidenced by ED.

Recently, $4a\times3b\times c$ superstructure was reported for the intercalated CoS, $[Co(en)_3](CoS)_{12}\cdot en$, crystallizing in polar $Pca2_1$ space group.[29] The structure was determined by means of single crystal X-ray diffraction. Renormalizing the composition to 10 S atoms results in $[Co_{10}S_{10}][Co(en)_3]_{0.83}\cdot en_{0.83}$ which is close but not identical to proposed in current work composition for compound **2**, $[Fe_{9.4(2)}S_{10}][Fe(en)_3]_{0.6(1)}\cdot en_{0.9(3)}$. The main difference between Co

and Fe compounds is that the Co-S layer is fully occupied, and no Co vacancies are present, plus the ratio of intercalated en and tris-en complexes is 1:1 for the Co compound.[29]

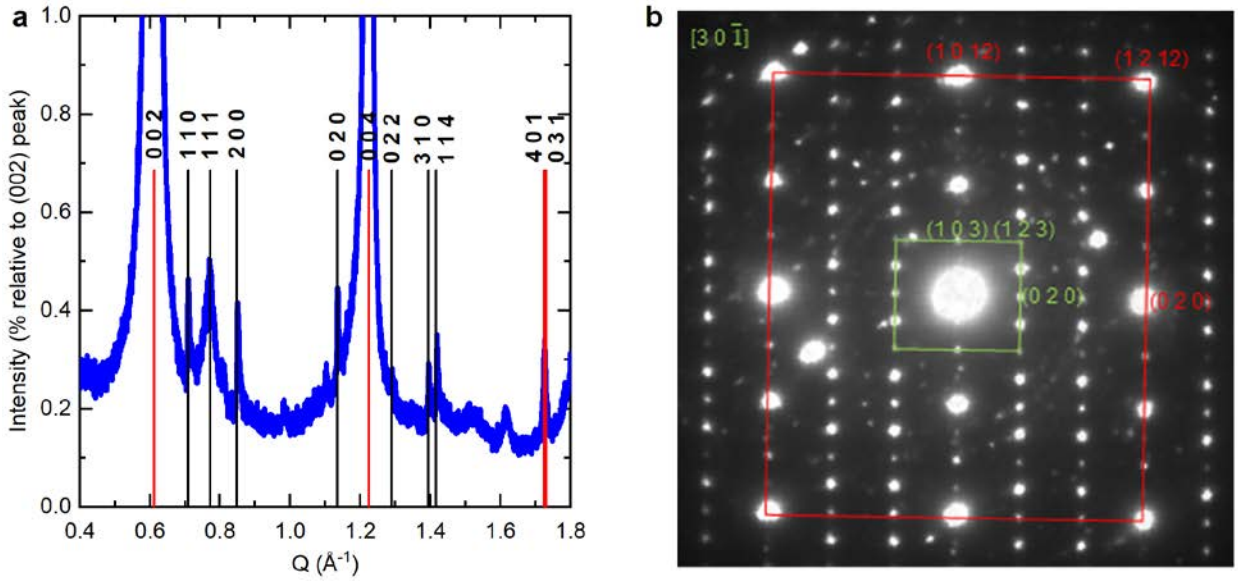

Figure 7. (a) *Low Q region of high resolution PXRD pattern of compound* ***2****. Red ticks correspond to a subcell a×b×c, 3.69×3.70×20.51 Å*^{3}*. Sharpest superstructural peaks are indexed by a 3a×4b×c supercell (black ticks). Miller indices are shown in black for supercell. Y axis is scaled to percentage of most intense peak, (002).* ***(b)*** *Electron diffraction image from* $[30\bar{1}]$ *zone axis indexed in the a×b×c subcell (red) and in the 4a×3b×c supercell (green).*

An expanded *ab*-plane could highlight vacancy ordering in the Fe-S layer or order within the intercalate or both as was observed in the crystal structure of compound **1**. For comparison, compound **1** contains four $[Fe(en)_3]^{2+}$ complexes and two free ethylenediamine molecules along the *ab*-plane of $\sqrt{5}a \times 4\sqrt{5}b$, 8.4×33.2 Å^2. From intralayer S···S distances, we can extrapolate that a $[Fe(en)_3]_2$·en unit fills an interlayer volume of approximately 1030 Å^3. In compound **2**, a $4a \times 3b \times c$ supercell has an interlayer volume of approximately 1270 Å^3. Assuming similar intercalate packing, the supercell would hold a single $[Fe(en)_3]_2$·en unit leaving ~25% open for

excess ethylenediamine, which would not fit an additional $Fe(en)_3$ complex but could fit extra ethylenediamine molecules. This falls in line with our determined composition where $Fe(en)_3$:free en ratio is 2:3, $[Fe_{9.4}S_{10}][Fe(en)_3]_{0.6}\cdot en_{0.9}$.

Ethylenediamine has a weak ligand field and $[Fe(en)_3]^{2+}$ complexes are expected to be high spin. For chain-like Fe-Se compound with $[Fe(en)_3]^{2+}$ intercalated species the high spin Fe^{2+} in the complex was confirmed by analysis of Fe-N distances in the crystal structure and ^{57}Fe Mössbauer spectroscopy.[30] We can assign formal oxidation state for compound **1**, assuming electron balance due to reported semiconducting properties: $[(Fe_8)^{18+}(S^{2-})_{10}][Fe(en)_3]^{2+}{}_1\cdot(en^0)_{0.5}$. This indicated average oxidation state of Fe in the Fe-S layer as +2.25. Following similar assignments for compound **2**, $[(Fe_{9.4})^{18.8+}(S^{2-})_{10}][Fe(en)_3]^{2+}{}_{0.6}\cdot(en^0)_{0.9}$ the expected oxidation state for Fe in the Fe-S layer is +2. To verify such description, ^{57}Fe Mössbauer spectroscopy was applied.

^{57}Fe Mössbauer Spectroscopy

^{57}Fe Mössbauer spectroscopy measurements were performed at 6 K, 100 K, and 293 K (**Figure 8**). An ~11% elemental Fe impurity was detected in compound **2**. Residual Fe was not removed from the sample studied by the Mössbauer spectroscopy because elemental Fe signal is well resolved. At room temperature, besides the signal of elemental Fe, two main contributions were observed. One of them is assigned to high-spin octahedral Fe^{2+} with a high isomer shift of ~1 mm/s and quadrupole splitting of 0.77 mm/s. The quadrupole splitting is strongly temperature dependent and at 6 K the same signal has values of $\delta = 1.12$ mm/s and $\Delta E = 1.54$ mm/s. Such values are typical for high spin Fe^{2+} in octahedral coordination.[30,31]

A second signal with substantially lower isomer shift (0.47 mm/s at room temperature) and low quadrupole splitting (0.21 mm/s at room temperature) can be assigned to tetrahedral Fe^{2+} in analogy to reported spectra for the chalcogenide compounds where Fe*Ch*$_4$ tetrahedra are fused

together and an extended network of Fe-Fe bonds is present. For example, in mackinawite and β-FeSe the reported isomer shifts for Fe^{2+} are 0.21 mm/s and 0.46-0.55 mm/s, respectively.[32-35] At 100 K, the signal of tetrahedral Fe splits into two components, the minor tetrahedral component exhibits hyperfine splitting indicating local magnetic ordering. At 6 K, the spectrum is best described with three tetrahedral Fe components, two are magnetically split and one major still a non-magnetic doublet (**Figure 8 and Table S3**). This behavior is reminiscent of the behavior of air-exposed FeSe samples, which also show a mixture of Fe^{2+} non-magnetic main component and magnetically split sextets.[32-33] In the case of air-exposed FeSe the partial magnetic ordering above 80 K was not detectable by magnetization measurements. This is also the case for compound **2**, at least for magnetization measurements performed at 1 T applied field (**Figure S8** and discussion of magnetic data below). This might be due to only a small fraction of tetrahedral Fe^{2+} (1/5) exhibits hyperfine splitting. Note that the Mössbauer sample was prepared under inert atmosphere of the glovebox with air- and moisture-free solvents and subsequently packed under Ar. Compound **2** has small amount (6%) of Fe vacancies in the FeS layer, which differentiate this layer from the stoichiometric superconducting FeS layer in mackinawite.

The relative ratio of tetrahedral/octahedral Fe signals (94:6) was used to guide the composition of compound **2** as described above. This ratio changes with temperature due to the different recoil-free fractions of two types of Fe species. The increase of the quadruple splitting for octahedral Fe with decreasing temperature was reported before for hybrid compounds with $[Fe(en)_3]^{2+}$ complexes such as $[Fe(en)_3]_3(FeSe_2)_4Cl_2$ as well as in Fe-containing MOFs.[30,36] A possible explanation was proposed upon studies of Fe-MOF-5, the strong temperature dependence of the quadrupole splitting was attributed to a temperature-induced change in the electron density distribution over asymmetrically occupied degenerate orbital states of Fe^{2+}.[36]

Mössbauer spectra of compound **1** are drastically different (**Figure 8**, **Table S3**). The spectra have no detectable contribution of elemental Fe. At each temperature the spectrum of compound **1** can be described as a combination of two octahedral Fe signals with large isomer shifts, >1 mm/s, and three signals from tetrahedral Fe with isomer shifts less than 0.65 mm/s. At 6 K the non-magnetic octahedral component has very similar isomer shift and quadrupole splitting (1.13 mm/s and 1.60 mm/s, respectively) to signal from octahedral Fe^{2+} in compound **2** (Table S3). This is in line with presence of $[Fe(en)_3]^{2+}$ complexes in the interlayer space of both compounds. A fraction of octahedral Fe^{2+} signal is magnetically split (component δ_2), perhaps due to induced magnetic field from Fe-S layer. This is supported with the lowest values of the hyperfine field of this component (~10 T). The main difference for compound **1** is that one of the octahedral and all tetrahedral Fe signals are magnetically split into sextets indicating that this compound is already magnetically ordered at room temperature, in contrast to compound **2**. The accurate fit of such complex overlapping spectrum is challenging, the best attempt is described in detail in the **SI**. With decreasing temperature, no substantial changes in the spectrum were observed other than slightly increased isomer shifts values due to the second order Doppler effect and minute increase in magnetic hyperfine fields.[37-38] At 6 K, two of the tetrahedral components have isomer shifts of 0.50 mm/s and 0.62 mm/s, which are similar to the tetrahedral Fe^{2+} signal in compound **2**. Similar values of isomer shifts and hyperfine fields were reported for $Rb_2Fe_4Se_5$ compound, which has the Fe-Se layer with 20% of Fe vacancies.[39-40] The last component in the spectrum of compound **1** is quite different, with smaller magnetic hyperfine field and a significantly smaller isomer shift of 0.24 mm/s, which is close to the isomer shift for tetrahedral Fe^{3+} in various chalcogenides.[41] The relative intensities of components is Fe^{3+}_{tetr}:Fe^{2+}_{tetr}:Fe^{2+}_{oct} = 24:65:11 which is close to the expected electron-balanced composition for compound **1**, $[(Fe^{3+})_2(Fe^{2+})_6S^{2-}_{10}][Fe^{2+}(en)_3]_1en_{0.5}$.

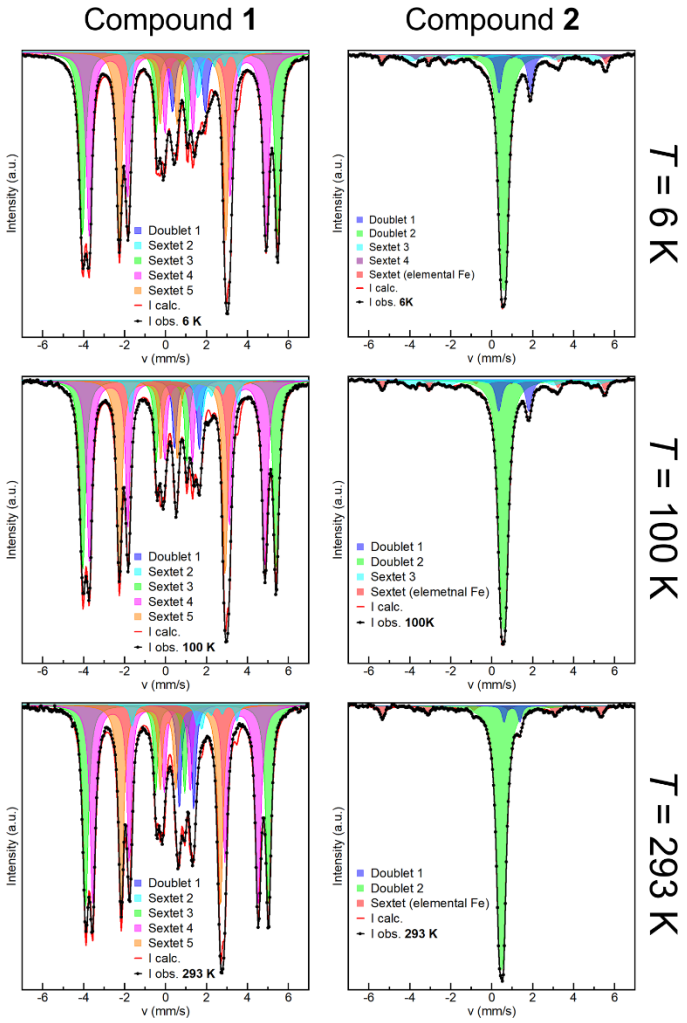

Figure 8. ^{57}Fe Mössbauer spectra for the Compound **1,** $[Fe_8S_{10}]Fe(en)_3 \cdot en_{0.5}$ (left panel) and Compound **2**, $[Fe_{9.4}S_{10}][Fe(en)_3]_{0.6} \cdot en_{0.9}$ (right panel) samples measured at 6 K, 100 K, and 293 K. The sub-spectra are also included.

^{57}Fe Mössbauer spectroscopy shows that compound **1** with ordered vacancies has a fraction of Fe^{3+} component in the Fe-S layer. Bond valance sum (BVS) method[42] estimates the average oxidation state across all intralayer Fe sites at +2.27(3), aligning with the expected $[(Fe^{3+})_2(Fe^{2+})_6S^{2+}_{10}]^{2-}$ distribution. As detailed in **Table S4**, BVS does not clearly distinguish any Fe^{3+} sites. Compound **1** is magnetically ordered above RT. Almost temperature-independent

magnetic hyperfine fields for the sextets (**Figure S6**) implies either a first order or second order phase transition at a temperature much higher than 300 K. High-temperature studies were precluded due to potential evaporation of en and S as indicated by TGA. In contrast, compound **2** with random placement of smaller amount of Fe vacancies in the flat Fe-S layer has no Fe^{3+} component in line with stoichiometric overall formula where all vacancies are compensated by interstitial Fe^{2+} complexes. Only partial magnetic ordering occurs in compound **2** well-below room temperature. The similarities of crystal structure of both studied compounds emphasize in the close values of isomer shift, quadrupole splitting, and hyperfine field for signals from octahedral $Fe^{2+}(en)_3$ and tetrahedral $Fe^{2+}S_4$.

Magnetic Properties

Compound 1

Compound **1** shows a Curie-Weiss-like temperature behavior of the magnetic susceptibility in the low applied fields down to base temperature of 2 K (**Figure S9**) with no signature of ordering and no indication of Fe-based impurities (**Figure S11**). Since Mössbauer spectroscopy reveals magnetic ordering at RT and no elemental Fe impurity was detected by the PXRD, magnetization data, and Mössbauer spectroscopy, no Honda-Owen's correction was applied. The data collected at 0.1 T applied field were fitted with modified Curie-Weiss law, $\chi = \chi_0 + C/(T-\theta)$. The Curie-Weis fit resulted in a negative Curie asymptotic temperature of –8.8(1) K and large χ_0 of 0.0328(4) emu/mol which is expected for a magnetically ordered system. The overall effective magnetic moment per 9 Fe atoms is small, 5.93(6) μ_B, and close to the expected localized moment for one equivalent of intercalated high-spin Fe^{2+} in the $Fe(en)_3$ complex, ~5.5 μ_B. Low thermal stability at elevated temperature prevented high-temperature magnetic study of compound **1**.

Temperature dependences of the magnetic susceptibility for compound **2** were measured at different applied magnetic fields (**Figures S7**). At applied fields of 1 T no substantial deviations from typical Curie-Weiss behavior was observed down to base temperature of 2 K (**Figure S8**). Isothermal studies of the field dependence of magnetization show the presence of ferromagnetic impurity at room temperature (**Figure S10**). Assuming this is elemental Fe, the amount was estimated as 1.5 wt.-%. To account for potential presence of residual ferromagnetic Fe impurity the Honda-Owen's correction was applied, $\chi = (M_2 - M_1)/(H_2 - H_1)$. Data measured at highest applied fields of 6 T and 7 T were used (**Figure S7b**). A Curie-Weiss fit of the data in the 34-300 K temperature range resulted in a negative Curie asymptotic temperature of –12.6(4) K indicating antiferromagnetic nearest-neighbor interactions. The overall effective magnetic moment per 10 Fe atoms is small, 5.7(4) μ_B. Assuming that Fe^{2+} in the $Fe(en)_3$ interstitial complexes exhibits Curie-Weiss behavior, it will contribute ~$5.5 \cdot \sqrt{0.6} = 4.2$ μ_B, to the total effective moment for the formula of $[Fe_{9.6}S_{10}][Fe(en)_3]_{0.6}en_{0.9}$. This resulted in a low effective moment of (5.7-4.2)/√(9.4) = 0.5(1) μ_B/Fe in the Fe-S layer. Such low moment is not uncommon for extended Fe-chalcogenide fragments where significant quenching of Fe magnetic moment was reported.[14,30,43-44] Partial magnetic ordering detected by Mössbauer spectroscopy was not observed in the magnetization measurement at 1T applied magnetic field (**Figure S8**).

Conclusions

We have synthesized a new ethylenediamine intercalated iron sulfide, $[Fe_{9.4(2)}S_{10}][Fe(en)_3]_{0.6(1)} \cdot en_{0.9}$, and determined a model for crystal structure based on a collaborative analysis of its elemental composition, decomposition behavior, diffraction and total scattering, magnetization, and ^{57}Fe Mössbauer spectroscopy. The model was based on a systematic comparison to the known structures, $[Fe_8S_{10}]Fe(en)_3 \cdot en_{0.5}$ and tetragonal FeS. The new compound

has flat $Fe_{9.4}S_{10}$ layers, analogous to iron deficient tetragonal FeS, which are intercalated by $[Fe(en)_3]^{2+}$ complexes and free ethylenediamine molecules. In the previously studied $[Fe_8S_{10}]Fe(en)_3 \cdot en_{0.5}$ compound, the intralayer iron has an average $Fe^{2.25+}$ oxidation state, causing layer puckering and significant deviation from typical flat superconducting FeS or FeSe layers. In $[Fe_{9.4}S_{10}][Fe(en)_3]_{0.6} \cdot en_{0.9}$ a larger fraction of the interlayer space is occupied with neutral en molecules reducing the presence of charged $[Fe(en)_3]^{2+}$ species. This leads to the suppression of intralayer iron vacancies causing the Fe-S layer to flatten and more closely resemble layers in superconducting binary FeS. Interlayer species are not randomly oriented but probably ordered as evidenced by superstructural diffraction peaks in both high-resolution PXRD and ED. Summarizing the structural information and magnetic properties for compound **2**, we can attest that many, but, clearly and empirically, not all of the criteria considered to be important for achieving superconductivity are fulfilled: compound **2** has regular flat layers of almost regular FeS_4 tetrahedra; there is large, over 10 Å, interlayer separation; Fe has formal oxidation state of +2; and compound is not magnetically ordered at room temperature. At least one feature that is lacking is the 100% occupancy of the Fe atoms in the tetrahedral layer. The presence of ~6(2)% of Fe vacancies seems to be still substantial for suppressing superconductivity and induce partial magnetic ordering at low temperatures in compound **2**, in line with other studies of binary and ternary iron chalcogenides.

We hypothesized that further variation of the synthetic conditions may stabilize phases with smaller fraction of intercalated Fe complexes and, correspondingly, lower fraction of Fe vacancies in the Fe-S layer, which may lead either to appearance of superconductivity or a clearer understanding of what feature are needed for superconductivity. Our work shows an importance

of detailed characterization of the crystal structure of intercalated compounds to understand the origin of the observed properties and develop proper structure-properties relationships.

Supporting Information. Figures and tables pertinent to characterization techniques used: electron microscopy, energy dispersive X-ray spectroscopy, TGA, powder X-ray diffraction and total scattering, electron diffraction, Mössbauer spectroscopy, magnetic measurements, and bond valence sum calculations. This material is available free of charge via the Internet at http://pubs.acs.org.

AUTHOR INFORMATION

Corresponding Author

Dr. Kirill Kovnir, kovnir@iastate.edu

Author Contributions

The manuscript was written through contributions of all authors.

Funding Sources

This research was supported by National Science Foundation DMR-2003783 grant to KK. Magnetic characterization performed by R.A.R. and P.C.C. were supported by the Ames Laboratory, the US Department of Energy, Office of Science, Basic Energy Sciences, Materials Science and Engineering Division under contract No. DE-AC02-07CH11358. Use of the Advanced Photon Source, an Office of Science User Facility operated for the U.S. Department of Energy (DOE) Office of Science by Argonne National Laboratory, was supported by the U.S. DOE under Contract No. DE-AC02-06CH11357. This research used resources of the National Synchrotron Light Source II, a U.S. Department of Energy (DOE) Office of Science User Facility

operated for the DOE Office of Science by Brookhaven National Laboratory under Contract No. DE-SC0012704.

Acknowledgements

The authors thank Dr. Saul Lapidus (APS ANL) for help collecting high resolution synchrotron PXRD patterns, as well as Dr. Leighanne Gallington (APS ANL) and Dr. Daniel Olds (NSLS-II BNL) for their collection of mail-in synchrotron X-ray total scattering data. The authors also thank Dr. Brett Boote (ISU Chemical Instrumentation Facility) for training and assistance with TGA/DSC – MS/FTIR measurements, and Dr. Warren Straszheim for access to the SEM/EDS at MARL ISU.

References

1. Hsu, F. C.; Luo, J. Y.; Yeh, K. W.; Chen, T. K.; Huang, T. W.; Wu, P. M.; Lee, Y. C.; Huang, Y. L.; Chu, Y. Y.; Yan, D. C.; Wu, M. K., Superconductivity in the PbO-type structure alpha-FeSe. *Proc. Natl. Acad. Sci. U. S. A.* **2008,** *105* (38), 14262-14264.
2. Lai, X.; Zhang, H.; Wang, Y.; Wang, X.; Zhang, X.; Lin, J.; Huang, F., Observation of Superconductivity in Tetragonal FeS. *J. Am. Chem. Soc.* **2015,** *137* (32), 10148-10151.
3. Pachmayr, U.; Nitsche, F.; Luetkens, H.; Kamusella, S.; Bruckner, F.; Sarkar, R.; Klauss, H. H.; Johrendt, D., Coexistence of 3d-ferromagnetism and superconductivity in $[(Li_{1-x}Fe_x)OH](Fe_{1-y}Li_y)Se$. *Angew. Chem. Int. Ed. Engl.* **2015,** *54* (1), 293-297.
4. Burrard-Lucas, M.; Free, D. G.; Sedlmaier, S. J.; Wright, J. D.; Cassidy, S. J.; Hara, Y.; Corkett, A. J.; Lancaster, T.; Baker, P. J.; Blundell, S. J.; Clarke, S. J., Enhancement of the superconducting transition temperature of FeSe by intercalation of a molecular spacer layer. *Nat. Mater.* **2013,** *12* (1), 15-19.
5. Hosono, S.; Noji, T.; Hatakeda, T.; Kawamata, T.; Kato, M.; Koike, Y., New Intercalation Superconductor $Li_x(C_6H_{16}N_2)_yFe_{2-z}Se_2$ with a Very Large Interlayer-Spacing and T_c = 38 K. *J. Phys. Soc. Japan* **2014,** *83* (11), 113704.
6. Zhou, X.; Wilfong, B.; Liou, S.-C.; Hodovanets, H.; Brown, C. M.; Rodriguez, E. E., Proton and ammonia intercalation into layered iron chalcogenides. *Chem. Commun.* **2018,** *54,* 6895-6898.
7. Vivanco, H. K.; Rodriguez, E. E., The intercalation chemistry of layered iron chalcogenide superconductors. *J. Solid State Chem.* **2016,** *242*, 3-21.
8. Sun, H.; Woodruff, D. N.; Cassidy, S. J.; Allcroft, G. M.; Sedlmaier, S. J.; Thompson, A. L.; Bingham, P. A.; Forder, S. D.; Cartenet, S.; Mary, N.; Ramos, S.; Foronda, F. R.; Williams, B. H.; Li, X.; Blundell, S. J.; Clarke, S. J., Soft chemical control of superconductivity in lithium iron selenide hydroxides $Li_{1-x}Fe_x(OH)Fe_{1-y}Se$. *Inorg. Chem.* **2015,** *54* (4), 1958-1964.

9. Lynn, J. W.; Zhou, X.; Borg, C. K. H.; Saha, S. R.; Paglione, J.; Rodriguez, E. E., Neutron investigation of the magnetic scattering in an iron-based ferromagnetic superconductor. *Phys. Rev. B* **2015,** *92* (6), 060510.
10. Sedlmaier, S. J.; Cassidy, S. J.; Morris, R. G.; Drakopoulos, M.; Reinhard, C.; Moorhouse, S. J.; O'Hare, D.; Manuel, P.; Khalyavin, D.; Clarke, S. J., Ammonia-rich high-temperature superconducting intercalates of iron selenide revealed through time-resolved in situ X-ray and neutron diffraction. *J. Am. Chem. Soc.* **2014,** *136* (2), 630-633.
11. Gao, Z.; Zeng, S.; Zhu, B.; Li, B.; Hao, Q.; Hu, Y.; Wang, D.; Tang, K., A FeSe-based superconductor $(C_2H_8N_2)_xFeSe$ with only ethylenediamine intercalated. *Sci. China Mater.* **2018,** *61* (7), 977-984.
12. Hatakeda, T.; Noji, T.; Kawamata, T.; Kato, M.; Koike, Y., New Li-Ethylenediamine-Intercalated Superconductor $Li_x(C_2H_8N_2)_yFe_{2-z}Se_2$ with T_c = 45 K. *J. Phys. Soc. Japan* **2013,** *82* (12), 123705.
13. Noji, T.; Hatakeda, T.; Hosono, S.; Kawamata, T.; Kato, M.; Koike, Y., Synthesis and post-annealing effects of alkaline-metal-ethylenediamine-intercalated superconductors $A_x(C_2H_8N_2)_yFe_{2-z}Se_2$ (A = Li, Na) with Tc = 45 K. *Phys. C* **2014,** *504*, 8-11.
14. Stahl, J.; Shlaen, E.; Singer, H.; Johrendt, D., Systematic dimensional reduction of the layered beta-FeSe structure by solvothermal synthesis. *Dalton Trans.* **2018,** *47* (10), 3264-3271.
15. Jin, S.; Wu, X.; Huang, Q.; Wu, H.; Ying, T.; Fan, X.; Sun, R.; Zhao, L.; Chen, X., Two new parent compounds for FeSe-based superconducting phases. *arXiv preprint arXiv:1607.01103,* **2016**.
16. Wu, D.; Guo, Z.; Liu, N.; Zhou, L.; Mao, Y.; Wan, L.; Sun, F.; Yuan, W., A new intercalated iron sulfide $(C_2H_8N_2)_{0.4}Fe_2S_2$ from solvothermal route: Synthesis, structure and tunable magnetism. *Inorg. Chem. Commun.* **2018,** *91*, 72-76.
17. Harmer, C. P.; Pak, C.; Greenfield, J. T.; Adeyemi, A. N.; Gamage, E. H.; Kovnir, K., Non-innocent Intercalation of Diamines into Tetragonal FeS Superconductor. *ACS Appl. Energy Mater.* **2021,** *4* (1), 42-46.
18. Wu, M.; Rhee, J.; Emge, T. J.; Yao, H.; Cheng, J. H.; Thiagarajan, S.; Croft, M.; Yang, R.; Li, J., A low band gap iron sulfide hybrid semiconductor with unique 2D $[Fe_{16}S_{20}]^{8-}$ layer and reduced thermal conductivity. *Chem. Commun.* **2010,** *46* (10), 1649-1651.
19. Favre-Nicolin, V.; Cerny, R., FOX, 'free objects for crystallography': A modular approach to ab initio structure determination from powder diffraction. *J. Appl. Cryst.* **2002,** *35*, 734-743.
20. Toby, B.; Dreele, R., GSAS-II: The Genesis of a Modern Open-Source All-Purpose Crystallography Software Package. *J. Appl. Cryst.* **2013,** *46*, 544-549.
21. Juhas, P.; Davis, T.; Farrow, C. L.; Billinge, S. J. L., PDFgetX3: a rapid and highly automatable program for processing powder diffraction data into total scattering pair distribution functions. *J. Appl. Crystallogr.* **2013,** *46*, 560-566.
22. Farrow, C. L.; Juhas, P.; Liu, J. W.; Bryndin, D.; Bozin, E. S.; Bloch, J.; Proffen, T.; Billinge, S. J. L., PDFfit2 and PDFgui: computer programs for studying nanostructure in crystals. *J. Phys.: Condens. Matter* **2007,** *19* (33), 7.
23. Lagarec, K.; Rancourt, D. C., Recoil -- Mossbauer spectral analysis software for Windows. Department of Physics, University of Ottawa, Ottawa, ON, Canada, 1998, version 1.0.
24. Keller-Besrest, F.; Collin, G., Structural aspects of the α transition in stoichiometric FeS: Identification of the high-temperature phase. *J. Solid State Chem.* **1990,** *84* (2), 194-210.

25. Beauvais, M. L.; Chupas, P. J.; O'Nolan, D.; Parise, J. B.; Chapman, K. W. Resolving Single-layer Nanosheets as Short-lived Intermediates in the Solution Synthesis of FeS. *ACS Mater. Lett.* **2021,** *3,* 698-703.
26. Berner, R.A.Tetragonal Iron Sulfide. *Science*. **1962**, *137,* 669.
27. Koz, C.; Schmidt, M.; Borrmann, H.; Burkhardt, U.; Röβler, S.; Carrillo-Cabrera, W.; Schnelle, W.; Schwarz, U.; Grin, Yu. Synthesis and crystal growth of tetragonal β-$Fe_{1.00}Se$. *Z. anorg. allg. Chem.* **2014**, *640*, 1600-1606.
28. Millican, J.N.; Phelan, D.; Thomas, E.L.; Leao, J.B.; Carpenter, E. Pressure-induced effects on the structure of the Fe Se superconductor. *Solid State Commun.* **2009**, *149*, 707-710.
29. Zheng, H.; Wilfong, B. C.; Hickox-Young, D.; Rondinelli, J. M.; Zavalij, P. Y.; Rodriguez, E. E. Polar Ferromagnetic Metal by Intercalation of Metal–Amine Complexes. *Chem. Mater.* **2021,** *33,* 4936-4947.
30. Gamage, E. H.; Greenfield, J. T.; Unger, C.; Kamali, S.; Clark, J. K.; Harmer, C. P.; Luo, L.; Wang, J.; Shatruk, M.; Kovnir, K., Tuning Fe-Se Tetrahedral Frameworks by a Combination of $[Fe(en)_3]^{2+}$ Cations and Cl^- Anions. *Inorg. Chem.* **2020,** *59* (18), 13353-13363.
31. Kamusella, S.; To Lai, K.; Harnagea, L.; Beck, R.; Pachmayr, U.; Singh Thakur, G.; Klauss, H. H. 57Fe Mössbauer Spectroscopy on Iron Based Pnictides and Chalcogenides in Applied Magnetic Fields. *Phys. Status Solidi B* **2017,** *254,* 1600160.

32. Greenfield, J. T.; Kamali, S.; Lee, K.; Kovnir, K., A Solution for Solution-Produced *β*-FeSe: Elucidating and Overcoming Factors that Prevent Superconductivity. *Chem. Mater.* **2015,** *27* (2), 588-596.

33. McQueen, T. M.; Huang, Q.; Ksenofontov, V.; Felser, C.; Xu, Q.; Zandbergen, H.; Hor, Y. S.; Allred, J.; Williams, A. J.; Qu, D.; Checkelsky, J.; Ong, N. P.; Cava, R. J., Extreme sensitivity of superconductivity to stoichiometry in $Fe_{1+\delta}Se$. *Phys. Rev. B* **2009,** *79* (1), 014522.
34. Mullet, M.; Boursiquot, S.; Abdelmoula, M.; Génin, J.-M.; Ehrhardt, J.-J., Surface chemistry and structural properties of mackinawite prepared by reaction of sulfide ions with metallic iron. *Geochim. Cosmochim. Acta* **2002,** *66* (5), 829-836.
35. Vaughan, D. J.; Ridout, M. S., Mössbauer studies of some sulphide minerals. *J. Inorg. Nucl. Chem.* **1971,** *33* (3), 741-746.
36. Brozek, C. K.; Ozarowski, A.; Stoian, S. A.; Dincă, M. Dynamic Structural Flexibility of Fe-MOF-5 Evidenced by ^{57}Fe Mössbauer Spectroscopy. *Inorg. Chem. Front.* **2017,** *4,* 782-788.
37. Tarras-Wahlberg, N.; Kamali, S.; Andersson, M.; Johansson, C.; Rosén, A., Magnetization and Mössbauer study of partially oxidized iron cluster films deposited on HOPG. *J. Magn. Magn. Mater.* **2014,** *367*, 40-46.
38. Mørup, S.; Madsen, D. E.; Frandsen, C.; Bahl, C. R. H.; Hansen, M. F., Experimental and theoretical studies of nanoparticles of antiferromagnetic materials. *J. Phys.: Condens. Matter* **2007,** *19* (21), 213202.
39. Ksenofontov, V.; Medvedev, S.A.; Schoop, L.M.; Wortmann, G.; Palasyuk, T.; Tsurkan, V.; Deisenhofer, J.; Loidl, A.; Felser, C. Superconductivity and magnetism in $Rb_{0.8}Fe_{1.6}Se_2$ under pressure. *Phys. Rev. B* **2012,** *85,* 214519.
40. Ksenofontov, V.; Wortmann, G.; Medvedev, Tsurkan, V.; Deisenhofer, J.; Loidl, A.; Felser, C. Phase separation in superconducting and antiferromagnetic $Rb_{0.8}Fe_{1.6}Se_2$ probed by Mössbauer spectroscopy. *Phys. Rev. B* **2011,** *84,* 180508(R).
41. Taft, C. A.; Raj, D.; Danon, J., Charge distribution and covalency effects on Mössbauer parameters in $KFeS_2$. *J. Phys. Chem. Solids* **1975,** *36* (4), 283-287.

42. Zheng, H.; Langner, K.; Shields, G.; Hou, J.; Kowiel, M.; Allen, F.; Murshudov, G.; Minor, W., Data mining of iron(II) and iron(III) bond-valence parameters, and their relevance for macromolecular crystallography. *Acta Crystallogr. D* **2017,** *73*, 316-325.
43. Pak, C.; Kamali, S.; Pham, J.; Lee, K.; Greenfield, J. T.; Kovnir, K., Chemical excision of tetrahedral $FeSe_2$ chains from the superconductor FeSe: synthesis, crystal structure, and magnetism of $Fe_3Se_4(en)_2$. *J. Am. Chem. Soc.* **2013,** *135* (51), 19111-4.
44. Greenfield, J. T.; Pak, C.; Kamali, S.; Lee, K.; Kovnir, K., Control over connectivity and magnetism of tetrahedral $FeSe_2$ chains through coordination Fe–amine complexes. *Chem. Comm.* **2015,** *51* (25), 5355-5358.